

Low-Dimensional Model of Spatial Shear Layers

Mingjun Wei,^{1, a)} Bashar R. Qawasmeh,¹ Matthew Barone,²
Bart G. van Bloemen Waanders,² and Lin Zhou^{1, b)}

¹⁾*Department of Mechanical and Aerospace Engineering,
New Mexico State University, Las Cruces, U.S.A.*

²⁾*Sandia National Laboratories, Albuquerque, U.S.A.*

(Dated: 22 March 2011)

The aim of this work is to develop nonlinear low-dimensional models to describe vortex dynamics in spatially developing shear layers with periodicity in time. By allowing a free variable $g(x)$ to dynamically describe downstream thickness spreading, we are able to obtain base functions in a scaled reference frame and construct effective models with only a few modes in the new space. To apply this modified version of proper orthogonal decomposition (POD)/Galerkin projection, we first scale the flow along x direction (downstream) to match a template function. In the scaled space, the first POD mode can capture more than 80% energy for each frequency. However, to construct a Galerkin model, the second POD mode plays a critical role and needs to be included. Finally, a reconstruction equation for the scaling variable g is derived to relate the scaled space to physical space, where downstream spreading of shear thickness presents. Using only two POD modes at each frequency, our models captured most basic dynamics of shear layers, such as vortex roll-up (by one-frequency model) and vortex-merging (by two-frequency model). When arbitrary excitation at different harmonics is added to the model, we can clearly observe the promoting or delaying/eliminating vortex merging events as a result of *mode competition*, which is commonly shown in experiments and numerical simulations of shear layers.

PACS numbers: 47.15.St, 47.20.Ft, 47.27.ed

Keywords: Proper Orthogonal Decomposition; Galerkin projection; shear layer; mode competition

^{a)}Electronic mail: mjwei@nmsu.edu

^{b)}Also at: Modern Mechanics Department, University of Science and Technology of China, P. R. China.

I. INTRODUCTION

Free shear layers are often studied as model flow for its simplicity. Behaviors of temporally developing (TD) and spatially developing (SD) shear layers have been studied for several decades from theoretical, numerical, and experimental perspectives¹⁻⁴. However, shear flows are still too complex to directly apply dynamic systems and control theories which have been widely used to analyze and understand many simple mechanical systems. Though low-dimensional models have been proposed^{3,5} and succeeded in some applications, they are mainly phenomenological. The goal here is to develop low-dimensional models from direct projection of first-principle governing equations.

Based on a combination of POD/Galerkin projection method and symmetry reduction idea introduced from geometric mechanics, Wei and Rowley recently developed low-dimensional models for TD free shear layers⁶. A scaling factor $g(t)$ was introduced to factor out the thickness growth, so that, similar vortex structures at different thickness can be uniformly described. It should be pointed out that the scaling factor was introduced and calculated simultaneously with *no self-similarity pre-known*. Similar technique has been used for traveling solutions⁷ and self-similar solutions⁸.

However, when the same idea was applied on SD shear layers, many new challenges appeared from the difference, sometimes critical, between temporal and spatial development.⁹ First, since the self-similarity happens in the streamwise (x direction) for SD flows, a scaling factor $g(x)$ as a function of x becomes a natural choice for symmetry reduction. Second, the periodicity can only exist in time and normally be introduced through extra constraints (e.g. external forcing). Last, the derived low-order model for SD shear layers is an ordinary differential equation evolving in space instead of time. The main difficulty caused by the above differences is from the fact that Navier-Stokes equations are parabolic in time but *not parabolic in space*. The ellipticity in space makes any model marching in space ill-posed. Parabolized stability equations (PSE)¹⁰ and parabolized Navier-Stokes equations (PNS)¹¹ have opened new avenues to the analysis of the streamwise growth of linear and nonlinear disturbances in slowly varying shear flows such as boundary layers, jets, and far wakes. PSE boundary layers are in general not parallel and are valid for convectively unstable flows such as the mixing layers. PNS equations become mathematically hyperbolic/parabolic in streamwise direction under certain conditions for the streamwise velocity and the stream-

wise pressure gradient. It is worth noting that weak ellipticity still exists in both PSE and PNS. For thin boundary layer type of flows, including the mixing layer in our case, normal diffusion fluxes dominate their streamwise counterparts¹², so that, it is common to drop streamwise diffusion terms for any approximation and parabolization efforts along streamwise direction¹³. However, to obtain a simple model strictly evolving downstream, we take the effort further by neglecting the ellipticity from pressure constraint, though the sacrifice of mass conservation has to be made at the same time.

For spatially-developing shear layers, mode competition has been studied experimentally and numerically as a trademark problem for decades^{2,14}. It simply appears when single-frequency excitation is introduced to a shear layer with broadband background noise¹⁵. The artificial excitation promotes the dynamics of its own frequency, and, at the same time, suppresses/delays the appearance of dynamics at other frequencies. With or without being promoted by external excitation, such nonlinear interaction between the harmonics and subharmonics always exists and often plays an essential role in mixing layer dynamics¹⁶. In mixing layers the forcing frequency and forcing amplitude have significant effects on the vortex merging such as the number of vortices in each merging and the location of the merging¹⁷. Moreover, Ho and Huang¹⁴ defined the merging/pairing location as the position where the subharmonic frequency saturates and reaches its peak. They also explained that exciting the fundamental frequency suppresses the subharmonic growth and delays the vortex pairing, while exciting the subharmonic promotes the vortex pairing. In the present work, mode competition is investigated to test the robustness of our model and also serves as a first application.

The paper is arranged as follows. Direct numerical simulation of SD shear layers is described in section II. Equation parabolization for modeling and an extension with external body forces will be discussed in section III. Section IV will then describe the entire methodology of low-dimensional modeling for SD shear layers. The results with further comparison and discussions will be in section V.

II. SIMULATION OF SPATIALLY DEVELOPING SHEAR LAYERS

The flow considered in this paper is a two-dimensional free shear layer developing spatially as shown schematically in figure 1. With the characteristic length being the initial vorticity

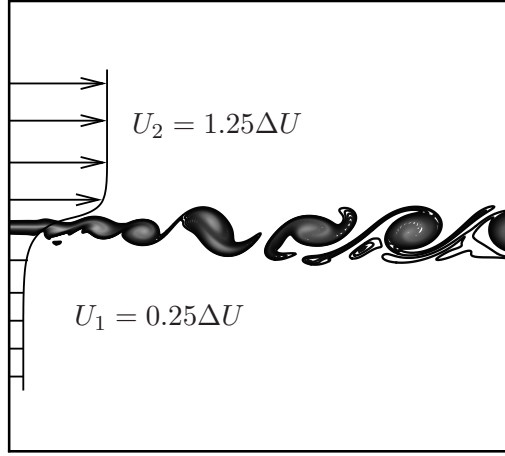


FIG. 1. Schematic of the two-dimensional free shear layer simulation.

thickness¹⁸ $\delta_\omega = \Delta U / |du/dy|_{\max}$ at the entrance and the characteristic velocity being the maximum velocity change across the shear layer ΔU , Reynolds number of the flow is $Re = 200$. All values are non-dimensionalized by the same characteristic values for the rest of the paper. Though the modeling will be based on the equations derived from incompressible Navier-Stokes equations, the simulation itself solves the fully compressible Navier-Stokes equations at low Mach number (convective Mach number is 0.3 in average), using a code that has been validated in previous work^{6,19}. The velocity divergence induced by weak compressibility here is small, and therefore has negligible impact on current modeling if no compressibility-specific features (e.g. acoustics) are considered. The usage of weakly-compressible data for incompressible modeling is common and has been successfully applied in our previous work on temporally-developing shear layers⁶.

The flow is simulated in a domain extending 200 in x and out to ± 80 in y from the mixing layer. Extra buffer areas with 20 at the top and bottom and 60 to the left and right are applied in the computation. To make the flow periodic in time, we seed bodyforce excitation in a small box area $5 < x < 15$, $-5 < y < 5$ to trigger the instability. Two excitation frequencies $k = 1$ and $k = 2$ are picked based on non-dimensional time period $T = 38.4$ for later analysis. For the chosen parameters, at the initial stage, the frequency $k = 2$ is near the the most unstable frequency predicted by linear instability, and $k = 1$ is getting more stable as the thickness getting thicker later²⁰.

III. PARABOLIZATION OF GOVERNING EQUATIONS

The governing equations for two-dimensional incompressible flow are

$$\begin{aligned} \frac{\partial u}{\partial x} + \frac{\partial v}{\partial y} &= 0 \\ \frac{\partial u}{\partial t} + u \frac{\partial u}{\partial x} + v \frac{\partial u}{\partial y} &= -\frac{\partial p}{\partial x} + \frac{1}{Re} \left(\frac{\partial^2 u}{\partial x^2} + \frac{\partial^2 u}{\partial y^2} \right) \\ \frac{\partial v}{\partial t} + u \frac{\partial v}{\partial x} + v \frac{\partial v}{\partial y} &= -\frac{\partial p}{\partial y} + \frac{1}{Re} \left(\frac{\partial^2 v}{\partial x^2} + \frac{\partial^2 v}{\partial y^2} \right). \end{aligned} \quad (1)$$

Mathematically, the elliptic behavior in space is introduced in two manners: 1) the Laplacian of velocity in viscous terms; and 2) pressure Poisson equation implied by the pressure terms and the continuity equation. The first one can be removed in a relatively easy way by assuming a thin layer^{12,21}, which ignores all $d^2(\cdot)/dx^2$ terms. For the second one, with the outer flow $U(x)$ being a function of x only, the thin-layer assumption can also remove the pressure effects. The momentum equations become

$$\begin{aligned} \frac{\partial u}{\partial t} + u \frac{\partial u}{\partial x} + v \frac{\partial u}{\partial y} &= \frac{1}{Re} \frac{\partial^2 u}{\partial y^2} \\ \frac{\partial p}{\partial y} &= 0. \end{aligned} \quad (2)$$

However, equation (2) loses the instability features^{22,23} required to initiate/terminate basic vortex dynamics. So, we put most of terms back in y momentum equation while still assuming negligible effects from pressure gradient and $d^2(\cdot)/dx^2$ terms for a thin layer. Thus, the reduced parabolic equations for later modeling are

$$\begin{aligned} u \frac{\partial u}{\partial x} &= -v \frac{\partial u}{\partial y} - \frac{\partial u}{\partial t} + \frac{1}{Re} \frac{\partial^2 u}{\partial y^2} \\ u \frac{\partial v}{\partial x} &= -v \frac{\partial v}{\partial y} - \frac{\partial v}{\partial t} + \frac{1}{Re} \frac{\partial^2 v}{\partial y^2}, \end{aligned} \quad (3)$$

where terms are rearranged for convenience. It is understood that pressure can be viewed as a Lagrange multiplier in the momentum equations to re-enforce the continuity equation (mass conservation). The simplification in (3) apparently releases this constraint, that is, the system mass can drift away. In our previous modeling for TD shear flow, we noticed that the model without mass conservation²⁴ is less accurate than the model with mass conservation⁶. However, the mass drift is slow and does not ruin the dynamics entirely, and the model without mass conservation, in its simple form and low order, can still describe

basic vortex dynamics. For SD shear flow, a low-order model based on (3) is expected to represent all basic vortex dynamics. We want to emphasize that though Galerkin projection is based on the parabolized equation (3), the numerical simulation of flow field uses complete Navier-Stokes equations which assure the accuracy of base functions (modes).

For the need of flow control, excitation is normally introduced and modeled as body force terms in momentum equations. Following the same idea above, Navier-Stokes equations with body force excitation can be parabolized to

$$\begin{aligned} u \frac{\partial u}{\partial x} &= -v \frac{\partial u}{\partial y} - \frac{\partial u}{\partial t} + \frac{1}{\text{Re}} \frac{\partial^2 u}{\partial y^2} + f_u(y, t) \\ u \frac{\partial v}{\partial x} &= -v \frac{\partial v}{\partial y} - \frac{\partial v}{\partial t} + \frac{1}{\text{Re}} \frac{\partial^2 v}{\partial y^2} + f_v(y, t), \end{aligned} \quad (4)$$

where, for simplicity, we assume excitation forces f_u and f_v being functions of y and t only. Based on (4), we can extend low-dimensional models to include the effects from external controls. Such extension serves as both an application and a test for model robustness as shown later.

IV. LOW-DIMENSIONAL MODELS

A. Scaling the flow dynamically

A common approach for low-dimensional modeling is to project governing equations onto a fixed set of basis functions, which are determined mathematically (i.e. Fourier modes) or empirically (i.e. POD modes). Here, since the shear layer thickness is spreading downstream in a manner of slow variation, we consider basis functions that can scale in y -direction to accommodate the spreading. A similar idea has been successfully applied on temporally-developing periodic shear flows^{6,24}. The main difference of the current scaling is that the scaling function becomes a function of x instead of t by its spatially-developing nature. If the velocity vector is defined by $\mathbf{q} = (u \ v)^T$, a scaled variable $\tilde{\mathbf{q}}$ can be introduced by

$$\mathbf{q}(x, y, t) = \tilde{\mathbf{q}}(x, g(x)y, t), \quad (5)$$

where $g(x)$ is a scaling factor to be determined. The purpose of introducing $g(x)$ is to factor out the mean flow development so that the flow dynamics can be represented by much fewer modes. Consequently, $g(x)$ is defined here to line up the scaled solution $\tilde{\mathbf{q}}$ the best to a

pre-selected template function. The initial shear flow profile $\mathbf{q}_0 = (u_0, v_0)$ can be a natural choice for this template, where

$$u_0 = U_1 + \frac{U_2 - U_1}{2}(1 + \tanh(2y)), \quad v_0 = 0. \quad (6)$$

It is noticed that the only non-zero component in the template is u_0 , the scaling factor $g(x)$ is therefore defined by

$$g(x) = \arg \min_g \|u^2(x, \frac{y}{g}, t) - u_0^2(y)\|^2, \quad (7)$$

where $\|\cdot\|^2$ is an L^2 norm defined upon the integration over y and single time period. A new thickness δ_g can be defined by $g(x)$ as

$$\delta_g = 1/g(x), \quad (8)$$

which can be used to measure the shear layer spreading as an alternative to vortex thickness or momentum thickness. In fact, all three thicknesses represent the shear layer spreading in a qualitatively similar way. The condition for $\tilde{u}(x, y, t) := u(x, y/g, t)$ to always match the template the best is

$$\left. \frac{d}{ds} \right|_{s=0} \|\tilde{u}^2(x, y, t) - u_0^2(h(s)y)\|^2 = 0, \quad (9)$$

where $h(s)$ is any curve in \mathbb{R}^+ with $h(0) = 1$, and the same norm on the space of functions of (y, t) is used: that is, $h = 1$ is a local minimum of the error norm above. Here \tilde{u}^2 is used instead of \tilde{u} as the way in our previous work for both TD⁶ and SD⁹ shear flows. The new choice simplifies the modeling of convective term $u\partial u/\partial x$ for SD flows, and results in a simpler and more accurate equation for $g(x)$. This expression (9) gives

$$-2 \left\langle \left. \frac{d}{ds} \right|_{s=0} u_0^2(h(s)y), \tilde{u}^2(x, y, t) - u_0^2(y) \right\rangle = 0$$

which becomes

$$\left\langle yu_0 \frac{\partial u_0}{\partial y}, \tilde{u}^2 - u_0^2 \right\rangle = 0. \quad (10)$$

Geometrically, the result in (10) means that the set of all such functions \tilde{u}^2 that are scaled so that they most closely match the template u_0^2 is an affine space through u_0^2 and orthogonal to $yu_0\partial u_0/\partial y$.

B. Equations in scaled space

We regard the parabolized equations as a dynamical system evolving on a function space H , consisting of the flow variables at (y, t) marching in x . Thus, $\mathbf{q}(x) \in H$ is a snapshot of the entire flow at location x , and equations (3) may be written as

$$\mathbf{A} \frac{\partial \mathbf{q}(x)}{\partial x} = h(\mathbf{q}(x)), \quad (11)$$

where

$$\mathbf{A} = \begin{bmatrix} u & 0 \\ 0 & u \end{bmatrix}, \quad (12)$$

to form the left-hand-side of (3), and h is a differential operator on H such that $h(\mathbf{q}(x))$ gives all right-hand-side terms of (3). Here matrix \mathbf{A} can also be written in scaled variables as

$$\tilde{\mathbf{A}} = \begin{bmatrix} \tilde{u} & 0 \\ 0 & \tilde{u} \end{bmatrix}, \quad (13)$$

and the same scaling holds as

$$\mathbf{A}(x, y, t) = \tilde{\mathbf{A}}(x, g(x)y, t). \quad (14)$$

If we introduce the scaling operator $S_g : H \rightarrow H$, defined by

$$S_g[\mathbf{q}(y, t)] = \mathbf{q}(gy, t), \quad \forall g \in \mathbb{R}^+ \quad (15)$$

then the scaling (5) becomes $\mathbf{q} = S_g[\tilde{\mathbf{q}}]$, (14) becomes $\mathbf{A} = S_g[\tilde{\mathbf{A}}]$, and the governing equations (11) may be written

$$S_{g(x)}[\tilde{\mathbf{A}}(x, y, t)] \frac{\partial}{\partial x} S_{g(x)}[\tilde{\mathbf{q}}(x, y, t)] = h(S_g[\tilde{\mathbf{q}}(x, y, t)]). \quad (16)$$

Since

$$\begin{aligned} \frac{\partial}{\partial x} S_{g(x)}[\tilde{\mathbf{q}}(x, y, t)] &= \frac{\partial}{\partial x} \tilde{\mathbf{q}}(x, g(x)y, t) \\ &= \frac{\partial \tilde{\mathbf{q}}}{\partial x}(x, gy, t) + \dot{g}y \frac{\partial \tilde{\mathbf{q}}}{\partial y}(x, gy, t) \\ &= S_g \left[\frac{\partial \tilde{\mathbf{q}}}{\partial x} \right] + \frac{\dot{g}}{g} S_g \left[y \frac{\partial \tilde{\mathbf{q}}}{\partial y} \right], \end{aligned} \quad (17)$$

(16) becomes

$$S_g[\tilde{\mathbf{A}}] S_g \left[\frac{\partial \tilde{\mathbf{q}}}{\partial x} \right] = h(S_g[\tilde{\mathbf{q}}]) - S_g[\mathbf{A}] \frac{\dot{g}}{g} S_g \left[y \frac{\partial \tilde{\mathbf{q}}}{\partial y} \right]. \quad (18)$$

If we define $S_{1/g}$ as an inverse mapping of S_g such that $h_g(\tilde{\mathbf{q}}) = S_{1/g}h(S_g[\tilde{\mathbf{q}}])$, applying the inverse mapping to above equation, we have the governing equations in scaled space

$$\tilde{\mathbf{A}} \frac{\partial \tilde{\mathbf{q}}}{\partial x} = h_g(\tilde{\mathbf{q}}) - \tilde{\mathbf{A}} \frac{\dot{g}}{g} y \frac{\partial \tilde{\mathbf{q}}}{\partial y}. \quad (19)$$

Equation (19) can be written separately in variables \tilde{u} and \tilde{v} as

$$\begin{aligned} \tilde{u} \frac{\partial \tilde{u}}{\partial x} &= h_g^1 - \frac{\dot{g}}{g} y \tilde{u} \frac{\partial \tilde{u}}{\partial y} \\ \tilde{u} \frac{\partial \tilde{v}}{\partial x} &= h_g^2 - \frac{\dot{g}}{g} y \tilde{u} \frac{\partial \tilde{v}}{\partial y}. \end{aligned} \quad (20)$$

However these equations alone are not sufficient to evolve the dynamics without the knowledge of $g(x)$.

C. Equation for scaling variable

In the section, the evolution equation for $g(x)$ will be derived to close the system. Differentiating the constraint (10) along x , we have

$$\left\langle y u_0 \frac{\partial u_0}{\partial y}, \tilde{u} \frac{\partial \tilde{u}}{\partial x} \right\rangle = 0. \quad (21)$$

Using the x -momentum equation (20):

$$\tilde{u} \frac{\partial \tilde{u}}{\partial x} = h_g^1 - \frac{\dot{g}}{g} y \tilde{u} \frac{\partial \tilde{u}}{\partial y}. \quad (22)$$

So that, we have

$$\left\langle y u_0 \frac{\partial u_0}{\partial y}, h_g^1 - \frac{\dot{g}}{g} y \tilde{u} \frac{\partial \tilde{u}}{\partial y} \right\rangle = 0, \quad (23)$$

which becomes

$$\frac{\dot{g}}{g} = \frac{\left\langle h_g^1, y u_0 \frac{\partial u_0}{\partial y} \right\rangle}{\left\langle y \tilde{u} \frac{\partial \tilde{u}}{\partial y}, y u_0 \frac{\partial u_0}{\partial y} \right\rangle}. \quad (24)$$

Altogether, equation (19) for $\tilde{\mathbf{q}}$ and equation (24) for g define the system evolution in a scaled space without slow variation from shear layer thickness.

D. Galerkin projection

Before we implement the projection, it is necessary to group the equations' right-hand-side into nonlinear terms \mathcal{N} , linear terms \mathcal{L} , and body force terms f_q which only appear

when external control is considered, as

$$h(\mathbf{q}) = \mathcal{N}(\mathbf{q}, \mathbf{q}) + \mathcal{L}(\mathbf{q}) + f_q, \quad (25)$$

where

$$\mathcal{N}(\mathbf{q}, \mathbf{q}) = \begin{bmatrix} -v \frac{\partial u}{\partial y} \\ -v \frac{\partial v}{\partial y} \end{bmatrix}, \quad \mathcal{L}(\mathbf{q}) = \begin{bmatrix} -\frac{\partial u}{\partial t} + \frac{1}{Re} \frac{\partial^2 u}{\partial y^2} \\ -\frac{\partial v}{\partial t} + \frac{1}{Re} \frac{\partial^2 v}{\partial y^2} \end{bmatrix}, \quad f_q = \begin{bmatrix} f_u \\ f_v \end{bmatrix}. \quad (26)$$

The corresponding terms in the scaled space are

$$h_g(\tilde{\mathbf{q}}) = \mathcal{N}_g(\tilde{\mathbf{q}}, \tilde{\mathbf{q}}) + \mathcal{L}_g(\tilde{\mathbf{q}}) + f_{\tilde{\mathbf{q}}}, \quad (27)$$

where

$$\mathcal{N}_g(\tilde{\mathbf{q}}, \tilde{\mathbf{q}}) = \begin{bmatrix} -\tilde{v} g \frac{\partial \tilde{u}}{\partial y} \\ -\tilde{v} g \frac{\partial \tilde{v}}{\partial y} \end{bmatrix}, \quad \mathcal{L}_g(\tilde{\mathbf{q}}) = \begin{bmatrix} -\frac{\partial \tilde{u}}{\partial t} + \frac{1}{Re} g^2 \frac{\partial^2 \tilde{u}}{\partial y^2} \\ -\frac{\partial \tilde{v}}{\partial t} + \frac{1}{Re} g^2 \frac{\partial^2 \tilde{v}}{\partial y^2} \end{bmatrix}, \quad f_{\tilde{\mathbf{q}}} = \begin{bmatrix} f_{\tilde{u}} \\ f_{\tilde{v}} \end{bmatrix}. \quad (28)$$

We can then expand $\tilde{\mathbf{q}}$ and $f_{\tilde{\mathbf{q}}}$ in its base functions as

$$\tilde{\mathbf{q}} = \tilde{\mathbf{q}}_0(y) + \sum_{k=-\infty}^{+\infty} \sum_{n=0}^{\infty} a_{k,n}(x) \Phi_{k,n}(t, y). \quad (29)$$

$$f_{\tilde{\mathbf{q}}} = \sum_{k=-\infty}^{+\infty} \sum_{n=0}^{\infty} A_{k,n} \Phi_{k,n}(t, y). \quad (30)$$

where

$$\Phi_{k,n}(t, y) = e^{2\pi i k t / T} \phi_{k,n}(y). \quad (31)$$

Here, k is the frequency, T is the time period, $a_{k,n}(x)$ are the POD coefficients, $\phi_{k,n} = (\hat{u}_{k,n}, \hat{v}_{k,n})$ is the n th POD mode for frequency k , and $A_{k,n}$ are the control force coefficients. Here, for simplicity, external control is arbitrarily assumed to be a combination of POD modes at different frequencies. The frequency and strength of external excitations can then be adjusted easily by altering the value of $A_{k,n}$. The energy of each POD mode (k, n) is quantified by

$$\lambda_{k,n} = \overline{|\langle \tilde{\mathbf{q}} - \tilde{\mathbf{q}}_0, \Phi_{k,n} \rangle|^2} = \overline{|a_{k,n}|^2}, \quad (32)$$

where $\bar{\cdot}$ denotes a streamwise spatial average.

We start with simple case retaining only frequencies $k = \pm 1$, and the first two POD modes $n = 1$ and $n = 2$ for each frequency. The summation is then an approximation of the

original $\tilde{\mathbf{q}}$. We will retain the notation $\tilde{\mathbf{q}}$ for the finite sum in (29). Since $\tilde{\mathbf{q}}$ must be real, we have the additional constraint that

$$a_{1,1}\Phi_{1,1} + a_{1,2}\Phi_{1,2} = a_{-1,1}^*\Phi_{-1,1}^* + a_{-1,2}^*\Phi_{-1,2}^* \quad (33)$$

which permits further simplification of the equations that follow.

To obtain the equations for coefficients $a_{1,1}(x)$ and $a_{1,2}(x)$, we project the governing equation (19) onto modes $\Phi_{1,1}$ and $\Phi_{1,2}$. Eventually, the spatial evolution equation for coefficient vector $\mathbf{a} = (a_{1,1} \ a_{1,2})^T$ is

$$\mathbf{B}\dot{\mathbf{a}} = (g\mathbf{C} + \mathbf{\Lambda} + \frac{1}{Re}g^2\mathbf{D} + \frac{\dot{g}}{g}\mathbf{E})\mathbf{a} + \mathbf{F}. \quad (34)$$

Matrices \mathbf{B} , \mathbf{C} , $\mathbf{\Lambda}$, \mathbf{D} , \mathbf{E} , and \mathbf{F} are defined by

$$\begin{aligned} \mathbf{B} &= \begin{bmatrix} b_{11} & b_{12} \\ b_{21} & b_{22} \end{bmatrix}, & \mathbf{C} &= \begin{bmatrix} c_{11} & c_{12} \\ c_{21} & c_{22} \end{bmatrix}, & \mathbf{\Lambda} &= \begin{bmatrix} c_{13} & 0 \\ 0 & c_{23} \end{bmatrix}, \\ \mathbf{D} &= \begin{bmatrix} d_{11} & d_{12} \\ d_{21} & d_{22} \end{bmatrix}, & \mathbf{E} &= \begin{bmatrix} e_{11} & e_{12} \\ e_{21} & e_{22} \end{bmatrix}, & \mathbf{F} &= \begin{bmatrix} A_{1,1} \\ A_{1,2} \end{bmatrix}, \end{aligned} \quad (35)$$

where all coefficients in matrices are well-defined and listed in appendix A with some detailed derivation. To close the system, the spatial evolution for thickness adjustment $g(x)$ is needed and can be obtained from scaling relation (24) with the same two modes being retained:

$$\dot{g} = \frac{(c_{01}a_{1,1}a_{1,1}^* + c_{02}a_{1,1}a_{1,2}^* + c_{03}a_{1,2}a_{1,1}^* + c_{04}a_{1,2}a_{1,2}^*)g^2 + \frac{1}{Re}d_0g^3}{b_0 + b_{01}a_{1,1}a_{1,1}^* + b_{02}a_{1,1}a_{1,2}^* + b_{03}a_{1,2}a_{1,1}^* + b_{04}a_{1,2}a_{1,2}^*}, \quad (36)$$

where all coefficients are also defined in appendix A. Having (36) together with (34), we are able to solve this low-dimensional model system.

If we choose two more modes $n = 1$ and 2 for wave number $k = 2$, the same derivation yields the equations for g , $a_{1,1}$, $a_{1,2}$, $a_{2,1}$, and $a_{2,2}$ to describe more complex physics. The resulting equations are lengthy, however, and are listed in appendix B.

V. RESULTS AND DISCUSSIONS

A. Basic model without artificial excitation

With the numerical configuration mentioned in section II, we start the simulation with excitations on hyperbolic tangent velocity profile and then allow a transition time for as

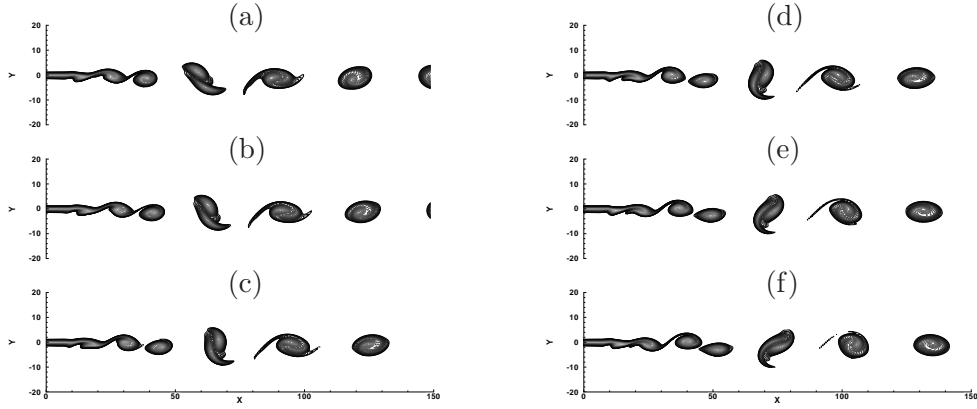


FIG. 2. Snapshots of the shear layer at different time: (a) $t = 50.4$; (b) $t = 60$; (c) $t = 69.6$; (d) $t = 79.2$; (e) $t = 88.8$; (f) $t = 98.4$. Contours show vorticity $|\omega| < 0.3$.

long as 10 periods of $k = 1$. Finally, another 10 periods are simulated and provide the data for mode decomposition. It is reminded that the natural excitations at frequencies $k = 1$ and $k = 2$ are only used to introduce instability to numerical simulation. So, these natural excitations are at very low amplitude and are not included in our model. They are different from the artificial excitations, which appear as extra terms in the model and are discussed in the next section.

Figure 2 shows several snapshots taken from the simulation, where typical dynamics such as vortex roll-up, pairing, and merging can be clearly observed. To have a more quantitative picture of the thickness growth, we compute δ_g thickness as the flow develops downstream (figure 3). It is easily observed that the thickness has overall growth with viscous spreading while showing events associated with vortices.

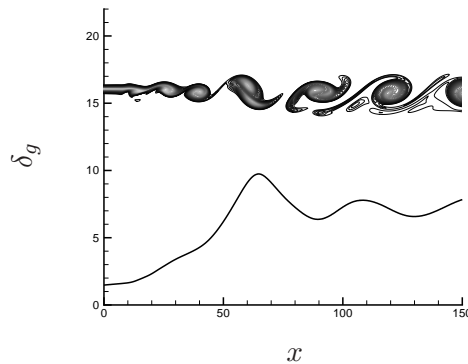


FIG. 3. The thickness growth along x direction while the shear layer is developing: sample vortex structure is shown for comparison.

The simulation data were then mapped to a scaled space with downstream thickness growth being factored out. In the scaled space, we can easily get POD modes for each time-frequency. Figure 4 shows the first and second \hat{v} POD modes at frequency $k = 1$. Comparing the \hat{v} modes in figure 4 to the instability mode at $k = 1$ (figure 5) from linear instability analysis³, we see the importance of POD mode $n = 2$ in forming a similar shape of the instability mode. There was a similar observation in modeling of TD flows⁶.

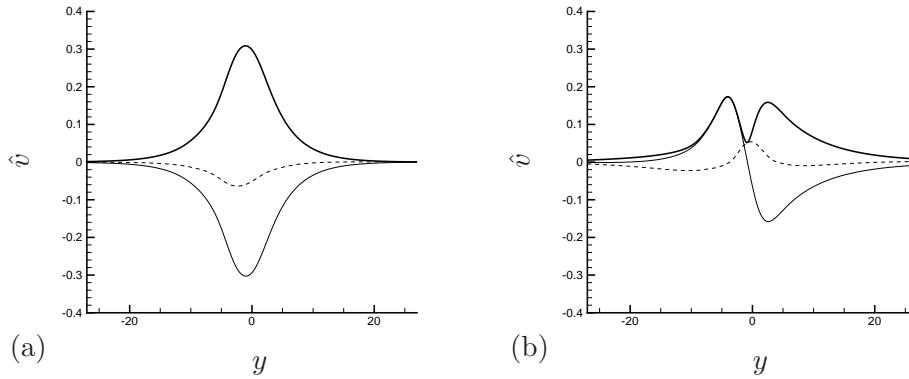


FIG. 4. \hat{v} for POD modes at $k = 1$: (a) $(k, n) = (1, 1)$ and (b) $(k, n) = (1, 2)$. The thin solid line represents the real value, the thin dashed line represents the imaginary value, and the thick solid line represents the absolute value.

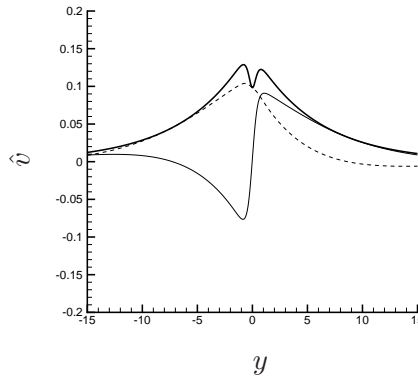


FIG. 5. \hat{v} of the instability mode for $k = 1$. The thin solid line represents the real value, the thin dashed line represents the imaginary value, and the thick solid line represents the absolute value.

For $k = 2$, first two POD modes are shown in figure 6. In a comparison to the instability mode at $k = 2$ (figure 7, the importance of including both POD modes at this frequency is implied in a similar way.

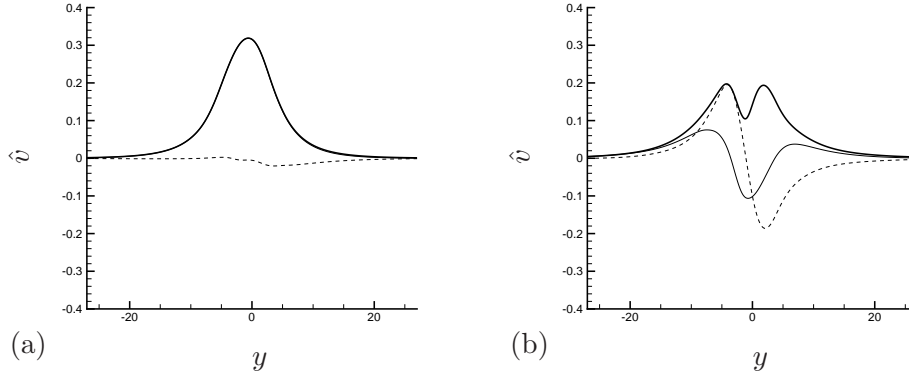


FIG. 6. \hat{v} for POD modes at $k = 2$: (a) $(k, n) = (2, 1)$ and (b) $(k, n) = (2, 2)$. The thin solid line represents the real value, the thin dashed line represents the imaginary value, and the thick solid line represents the absolute value.

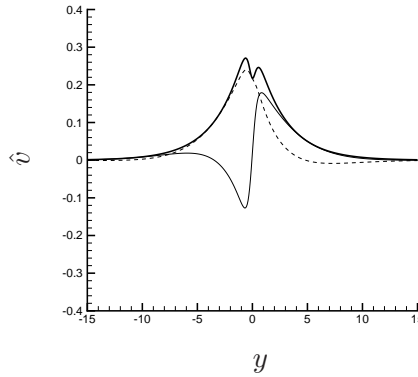


FIG. 7. \hat{v} of the instability mode for $k = 2$. The thin solid line represents the real value, the thin dashed line represents the imaginary value, and the thick solid line represents the absolute value.

Table I lists each modes' energy defined by (32). The first POD modes of each frequency contain most of the energy (totally 82.0% from modes (1,1) and (2,1)). However, as being indicated by the comparison to the instability modes, the second POD modes are dynamically important for the instability despite their much less energy (totally 7.5% by mode (1,2) and (2,2)).

The downstream evolution of these 4 POD modes can be therefore obtained by the projection of DNS data in the scaled space as shown in figure 8(a). As the flow developing downstream (along x), 2 POD modes at $k = 2$, as the most unstable modes for the initial shear thickness, at first dominate the dynamics. In a comparison to the thickness growth,

(k, n)	energy (%)	(k, n)	energy (%)
(1, 1)	67.6	(2, 1)	14.4
(1, 2)	5.0	(2, 2)	2.5

TABLE I. Energy captured by different POD modes.

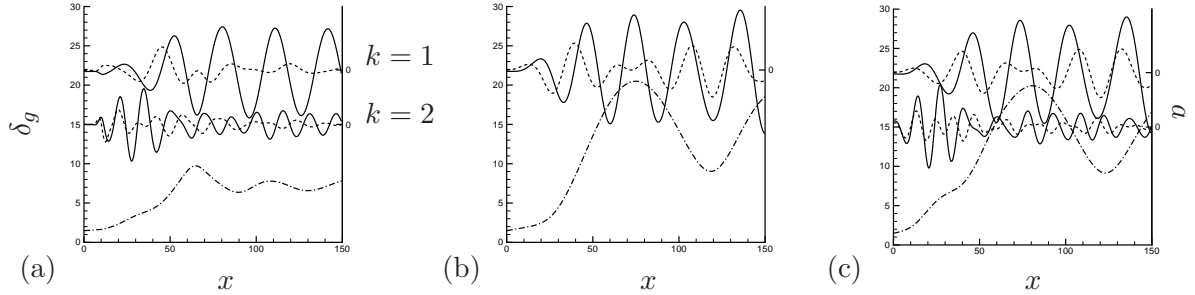


FIG. 8. Comparison of (a) direct projection from DNS data to (b) 2-mode model results and (c) 4-mode model results: —, real part of mode coefficient $a_{1,1}$ and $a_{2,1}$; ----, real part of mode coefficient $a_{1,2}$ and $a_{2,2}$; -·-·-, shear-layer thickness δ_g .

the growth of $k = 2$ modes has clear contribution to the initial thickness growth from $x = 10$ to $x = 40$. As the shear layer getting thicker, $k = 1$ modes become instead more unstable, and quickly take the dominant role. The appearance of $k = 1$ modes triggers a sharp increase of thickness from $x = 40$ to $x = 70$. On the other hand, $k = 2$ modes are suppressed by $k = 1$ modes through *mode competition*.

To get a 2-mode model for SD shear layers, we substitute the first and second POD modes of $k = 1$ into the coefficients and model equations defined respectively in appendix A and section IV, and evolve the model equations along x to get the coefficients $\mathbf{a}(x)$ and scaling function $g(x)$ as the flow develops downstream. Figure 8 compares the mode coefficients and δ_g thickness calculated from the 2-mode model (figure 8b) to the direction projection from DNS data (figure 8a). The model captures some basic dynamics: 1) overall thickness growth; 2) oscillation frequency and amplitude of each modes for $k = 1$. Of course, the 2-mode model with single frequency can not describe the thickness variation by the appearance of $k = 2$ vortices. The thickness variation by $k = 1$ vortices are captured but with amplified oscillation.

Similarly, to get a 4-mode (two-frequency) model, we substitute the first and second POD

modes of each frequency $k = 1$ and $k = 2$ into the coefficients defined in appendix B, and evolve the model equations along x to compute $\mathbf{a}(x)$ and $g(x)$. The 4-mode model results are also shown and compared in figure 8, where the mode coefficients and δ_g thickness calculated from the 4-mode model (figure 8c) are compared to the DNS data projection (figure 8a). This time, we successfully captured the oscillation of POD modes from both $k = 1$ and $k = 2$ frequencies. The inclusion of $k = 2$ contributes to the success of presenting a small variation of thickness caused by $k = 2$ vortices rolling-up, which is totally neglected by 2-mode model. However, there is no clear improvement for the over-estimation of thickness variation by $k = 1$ vortices.

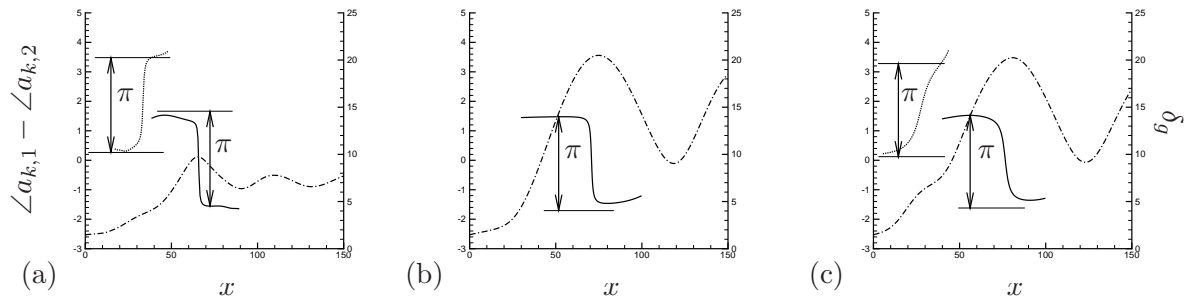


FIG. 9. Relation between the shear layer thickness variation and the sudden change of the phase difference of the first two POD modes: (a) from the projection of full simulation; (b) from the solution of 2-mode model; (c) from the solution of 4-mode model. Notations are: — phase difference between $a_{1,1}$ and $a_{1,2}$, phase difference between $a_{2,1}$ and $a_{2,2}$, and - - - - the shear layer thickness δ_g .

In figure 8, for both DNS projection and model results, the thickness growth lines show certain wavy behavior with overall viscous increase. Such local variation seems a result from the interaction between 2 POD modes at the same frequency. Figure 9 then gives a better understanding of such local changes by checking the phase difference between POD modes at the same frequency. It shows, for both DNS (figure 9a) and models (figures 9b and 9c), the sudden change of the thickness from increase to decrease is always accompanied by the sudden change of phase angle for 180° of the phase difference between the first and the second POD modes. This observation is true for both modes at $k = 1$ and $k = 2$. The models represent such phase angle change in the exact same way as the DNS. This relation between phase angle and local variation has also been reported in TD shear layers⁶.

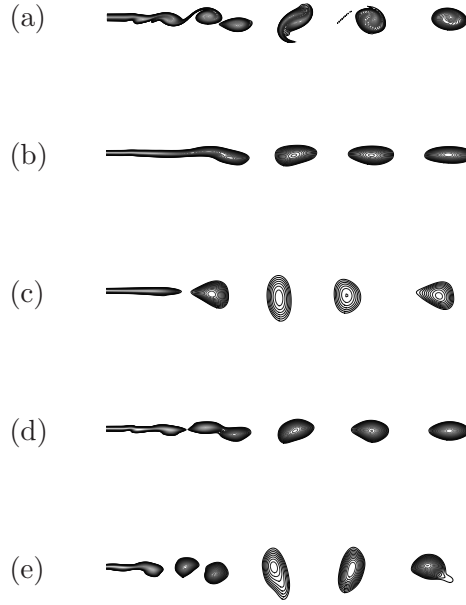


FIG. 10. Comparison of flow fields at time $t = 768$ visualized from: (a) DNS data; (b) projection of DNS data onto 2 POD modes at $k = 1$; (c) 2-mode model; (d) projection of DNS data onto all 4 modes; (e) 4-mode model;. Contours show vorticity $|\omega| < 0.3$.

To achieve a better physical understanding, figure 10 depicts the vorticity field and shows a comparison among the original simulation, the projection of simulation data onto 2 modes which is considered as an exact solution to compare with 2-mode model, the projection of simulation data onto 4 modes which is considered as an exact solution to compare with 4-mode model, and the results from 2-mode and 4-mode models. The 2-mode model shows the capability to describe the appearance of $k = 1$ large vortices. However, 2-mode model produces $k = 1$ vortices from direct roll-up instead of going through the pairing and merging process of smaller vortices at $k = 2$. It is from the lack of $k = 2$ information in the 2-mode model, and it is consistent with the direct projection from DNS data onto these two modes. By adding two more modes from frequency $k = 2$, the 4-mode model has the full capability to capture the whole process including roll-up, pairing, and merging of vortices in a way consistent with the DNS projection onto these 4 modes. In fact, most characteristics of the original simulation data are represented by these 4 modes. The over-estimation of thickness variation shown before in figure 8 now appears as vortices being over-stretched along y direction, however, without ruining basic vortex dynamics.

B. Forced model with artificial excitations

With the external control force being also considered in section IV, the model can be extended to study the response to artificial excitations at different frequencies. In shear layers, such frequency responses are often studied as *mode competition*. The competition for energy between modes at different frequencies is well-known in determining basic vortex dynamics (e.g. roll-up, pairing, and merging) in shear layers^{2,14–17,25–27}. Without external excitation, the competition between frequencies can be predicted by their instability feature; with external excitation, the forcing frequency, instead, determines the dominant frequency. In our study, we model the external excitation in the simplest form by assuming their spatial function the same as our base functions (i.e. POD modes) and the temporal frequencies at $k = 1$ and $k = 2$. So that, *without running corresponding numerical simulation*, the forced model is expected to predict similar behavior of mode competition as in real simulation of shear layers. With excitation at various amplitudes being introduced, we also provide a challenge to the model robustness.

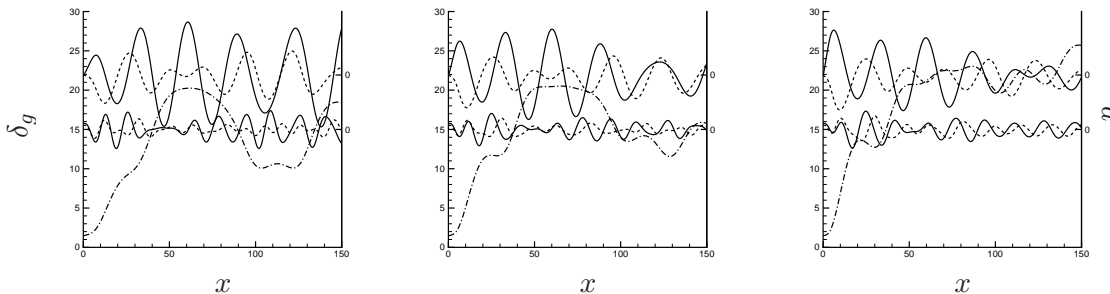


FIG. 11. Comparison of excitations at frequency $k = 1$ with mode (1,1): different amplitudes are applied at 0.5 (left) 1.0 (middle) and 1.5 (right); —, real part of mode coefficient $a_{1,1}$ and $a_{2,1}$; ----, real part of mode coefficient $a_{1,2}$ and $a_{2,2}$; - - - -, shear-layer thickness δ_g .

Since at least two frequencies need to be involved in mode competition, we only consider the 4-mode model in this section. For simplicity, only the first POD modes of each frequencies are considered in external forcing, though the excitation with the second POD modes can also change the vortex dynamics in a similar but less pronounced way. Figure 11 shows the results by exciting at $k = 1$ with mode (1,1). It is clearly shown that both POD modes at $k = 1$ are promoted and both modes at $k = 2$ are suppressed. The large peak

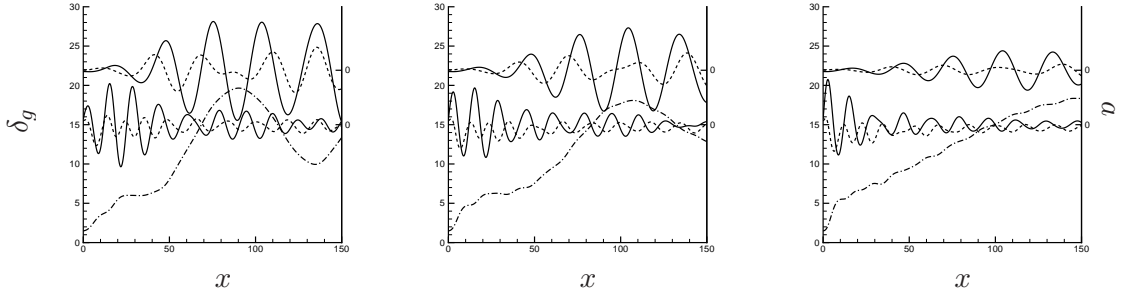


FIG. 12. Comparison of excitations at frequency $k = 2$ with mode (2,1): different amplitudes are applied at 1.0 (left) 2.0 (middle) and 3.0 (right): —, real part of mode coefficient $a_{1,1}$ and $a_{2,1}$; ----, real part of mode coefficient $a_{1,2}$ and $a_{2,2}$; - - - -, shear-layer thickness δ_g .

of the thickness growth, which is corresponding to the appearance of $k = 1$ vortex, is also moved towards the upstream. On the other hand, with the excitation at $k = 2$ with mode (2,1) (figure 12), the appearance of modes at $k = 1$ is significantly delayed. The rapid increase in the thickness is also pushed downstream and even disappears. For both figures, the excitations with larger amplitude amplify the behavior.

In figure 13, we reconstruct the vortex field from model computation so that the characteristics of mode competition are shown in a physical and more clear manner. In figure 13(a), snapshots from DNS projection to all 4 modes are used to show the whole evolution of vortex dynamics from roll-up, pairing, to merging. The stage for dominant frequency switching from $k = 2$ to $k = 1$ is identified by the entire vortex pairing/merging process and is boxed. Once vortex merging is completed, shear layer thickness reaches its peak and is noted by a vertical line in the picture below. The results from 4-mode model show similar behavior in figure 13(b). With excitation at $k = 1$, figure 13(c) shows clearly shortened pairing/merging stage and a promotion of vortex structures at $k = 1$. With excitation at $k = 2$, figure 13(d), on the other hand, shows a longer pairing/merging process and a delayed appearance of $k = 1$ vortices. Such behaviors have been observed experimentally and numerically^{2,14}, and here, they are qualitatively predicted by the current model without running extra simulations.

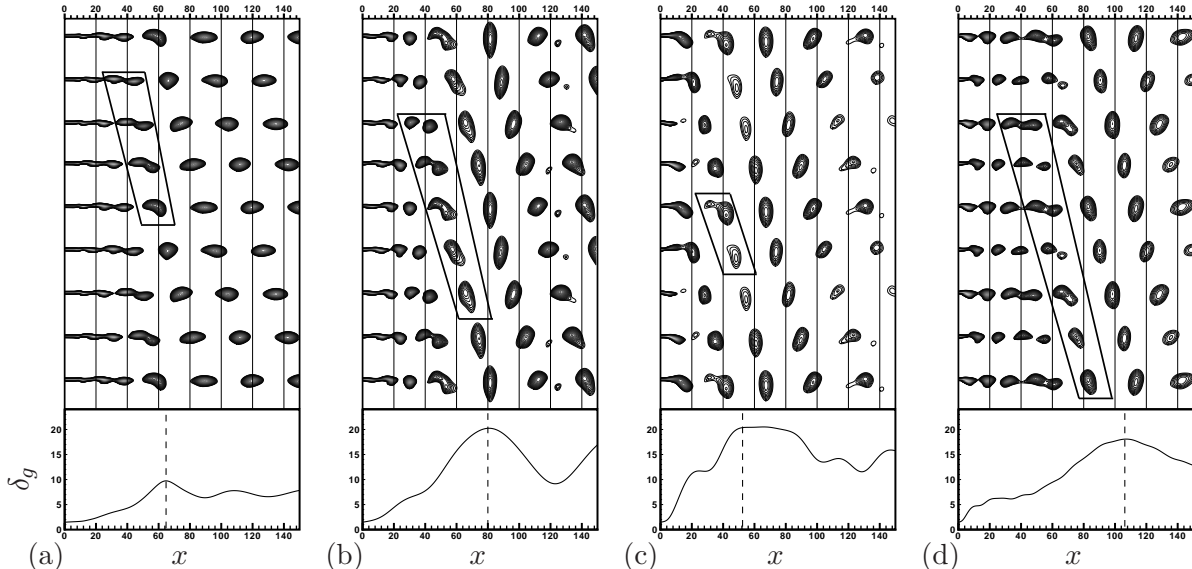


FIG. 13. Vorticity field snapshots (top) (at $t = 624, 648, 672, 696, 720, 744, 768, 792,$ and 816) and average thickness variations (bottom) from: (a) DNS projection on 4 modes; (b) 4-mode model; (c) 4-mode model with excitation at $k = 1$; (d) 4-mode model with excitation at $k = 2$. Contours show vorticity $|\omega| < 0.3$.

VI. CONCLUSION

Direct numerical simulation of a SD shear layer shows overall downstream spreading with events marked by vortex roll-up, pairing, and merging. When vortex structures translate downstream, most of these physical mechanisms remain present. However, this similarity can be damaged by the effects from mean flow variation along x , and therefore, the number of required modes increases in reduced-order modeling. In order to avoid this problem, we introduce a function $g(x)$ to scale the flow dynamically in y -direction so that the shear-layer thickness remains the same in the scaled space. Then, a low-dimensional system evolving downstream can be built more efficiently in the new symmetry-reduced space, using traditional POD/Galerkin projection. Finally, a reconstruction equation for $g(x)$ is derived and computed simultaneously to close the system.

The approach needs to be based on equations strictly parabolized along x and at the same time with enough terms to keep some key physics (i.e. instability). Such parabolic requirement is satisfied by applying a thin-layer assumption in a spatially-developing shear layer but without neglecting key terms for basic instability.

A 2-mode model for SD shear layers is developed to describe vortex roll-up and shear-layer thickness changes. Similar to TD cases, we need at least two POD modes for each frequency for a successful model. The shapes of each modes are also similar to those of TD cases, and therefore, a possible connection between the POD modes and the instability modes is indicated. The downstream development of each modes is depicted qualitatively well by the 2-mode model even without enforcing mass conservation. Similarly, a 4-mode model for SD shear layers is developed to describe more complex dynamics involving the interaction between harmonics (e.g. vortex pairing and merging). There is an overall improvement for the 4-mode model, but the thickness oscillation is still over-predicted due to lack of mass conservation. Similar differences due to absence/presence of mass conservation are observed for low-dimensional TD models.^{6,24}

With an extension to include effects from external excitation, the models can describe the response to different frequencies. The forced 4-mode model successfully predicts basic characteristics of mode competition without running the corresponding numerical simulations. The model also shows robustness under excitations at different amplitudes.

ACKNOWLEDGMENTS

We thank Professor Clancy Rowley for constructive discussion. MW and BQ also gratefully acknowledge the support from Sandia-University Research Program (SURP). Sandia is a multiprogram laboratory operated by Sandia Corporation, a Lockheed Martin Company for the United States Department of Energy's National Nuclear Security Administration under contract DE-AC04-94AL85000.

Appendix A: Equations and coefficients for the 2-mode model

1. Projection of left-hand-side

$$\begin{aligned} \left\langle \tilde{\mathbf{A}} \frac{\partial \tilde{\mathbf{q}}}{\partial x}, \Phi_{1,1} \right\rangle &= T \left[\int (u_0 \hat{u}_{1,1} \hat{u}_{1,1}^* + u_0 \hat{v}_{1,1} \hat{v}_{1,1}^*) dy \right] \dot{a}_{1,1} + T \left[\int (u_0 \hat{u}_{1,2} \hat{u}_{1,1}^* + u_0 \hat{v}_{1,2} \hat{v}_{1,1}^*) dy \right] \dot{a}_{1,2} \\ &= T(b_{11} \dot{a}_{1,1} + b_{12} \dot{a}_{1,2}), \end{aligned}$$

(A1)

so that coefficients are defined

$$b_{11} = \int (u_0 \hat{u}_{1,1} \hat{u}_{1,1}^* + u_0 \hat{v}_{1,1} \hat{v}_{1,1}^*) dy \quad (\text{A2})$$

$$b_{12} = \int (u_0 \hat{u}_{1,2} \hat{u}_{1,1}^* + u_0 \hat{v}_{1,2} \hat{v}_{1,1}^*) dy. \quad (\text{A3})$$

Similarly,

$$b_{21} = \int (u_0 \hat{u}_{1,1} \hat{u}_{1,2}^* + u_0 \hat{v}_{1,1} \hat{v}_{1,2}^*) dy \quad (\text{A4})$$

$$b_{22} = \int (u_0 \hat{u}_{1,2} \hat{u}_{1,2}^* + u_0 \hat{v}_{1,2} \hat{v}_{1,2}^*) dy. \quad (\text{A5})$$

2. Projection of nonlinear terms

$$\begin{aligned} \langle \mathcal{N}_g(\tilde{\mathbf{q}}, \tilde{\mathbf{q}}), \Phi_{1,1} \rangle &= -Tg \left[\int (\hat{v}_0 \frac{d\hat{u}_{1,1}}{dy} \hat{u}_{1,1}^* + \hat{v}_0 \frac{d\hat{v}_{1,1}}{dy} \hat{v}_{1,1}^*) dy \right] a_{1,1} \\ &\quad - Tg \left[\int (\hat{v}_0 \frac{d\hat{u}_{1,2}}{dy} \hat{u}_{1,1}^* + \hat{v}_0 \frac{d\hat{v}_{1,2}}{dy} \hat{v}_{1,1}^*) dy \right] a_{1,2} \\ &\quad - Tg \left[\int (\hat{v}_{1,1} \frac{d\hat{u}_0}{dy} \hat{u}_{1,1}^* + \hat{v}_{1,1} \frac{d\hat{v}_0}{dy} \hat{v}_{1,1}^*) dy \right] a_{1,1} \\ &\quad - Tg \left[\int (\hat{v}_{1,2} \frac{d\hat{u}_0}{dy} \hat{u}_{1,1}^* + \hat{v}_{1,2} \frac{d\hat{v}_0}{dy} \hat{v}_{1,1}^*) dy \right] a_{1,2} \\ &= -Tg \left[\int (\hat{v}_{1,1} \frac{d\hat{u}_0}{dy} \hat{u}_{1,1}^*) dy \right] a_{1,1} - Tg \left[\int (\hat{v}_{1,2} \frac{d\hat{u}_0}{dy} \hat{u}_{1,1}^*) dy \right] a_{1,2}, \\ &= Tg(c_{11}a_{1,1} + c_{12}a_{1,2}). \end{aligned} \quad (\text{A6})$$

where $\hat{v}_0 = 0$ is applied. So, we have

$$c_{11} = - \int (\hat{v}_{1,1} \frac{d\hat{u}_0}{dy} \hat{u}_{1,1}^*) dy \quad (\text{A7})$$

$$c_{12} = - \int (\hat{v}_{1,2} \frac{d\hat{u}_0}{dy} \hat{u}_{1,1}^*) dy. \quad (\text{A8})$$

Similarly,

$$c_{21} = - \int (\hat{v}_{1,1} \frac{d\hat{u}_0}{dy} \hat{u}_{1,2}^*) dy \quad (\text{A9})$$

$$c_{22} = - \int (\hat{v}_{1,2} \frac{d\hat{u}_0}{dy} \hat{u}_{1,2}^*) dy. \quad (\text{A10})$$

3. Projection of linear terms

$$\begin{aligned}
\langle \mathcal{L}_g(\tilde{\mathbf{q}}), \Phi_{1,1} \rangle &= -T \left(\frac{2\pi i}{T} \right) \left[\int (\hat{u}_{1,1} \hat{u}_{1,1}^* + \hat{v}_{1,1} \hat{v}_{1,1}^*) dy \right] a_{1,1} \\
&\quad + \frac{1}{Re} g^2 T \left\{ \left[\int \left(\frac{d^2 \hat{u}_{1,1}}{dy^2} \hat{u}_{1,1}^* + \frac{d^2 \hat{v}_{1,1}}{dy^2} \hat{v}_{1,1}^* \right) dy \right] a_{1,1} \right. \\
&\quad \left. + \left[\int \left(\frac{d^2 \hat{u}_{1,2}}{dy^2} \hat{u}_{1,1}^* + \frac{d^2 \hat{v}_{1,2}}{dy^2} \hat{v}_{1,1}^* \right) dy \right] a_{1,2} \right\}, \\
&= T (c_{13} a_{1,1} + \frac{g^2}{Re} [d_{11} a_{1,1} + d_{12} a_{1,2}]).
\end{aligned} \tag{A11}$$

that

$$c_{13} = -\left(\frac{2\pi i}{T} \right) \int (\hat{u}_{1,1} \hat{u}_{1,1}^* + \hat{v}_{1,1} \hat{v}_{1,1}^*) dy \tag{A12}$$

$$d_{11} = \int \left(\frac{d^2 \hat{u}_{1,1}}{dy^2} \hat{u}_{1,1}^* + \frac{d^2 \hat{v}_{1,1}}{dy^2} \hat{v}_{1,1}^* \right) dy \tag{A13}$$

$$d_{12} = \int \left(\frac{d^2 \hat{u}_{1,2}}{dy^2} \hat{u}_{1,1}^* + \frac{d^2 \hat{v}_{1,2}}{dy^2} \hat{v}_{1,1}^* \right) dy. \tag{A14}$$

Similarly

$$c_{23} = -\left(\frac{2\pi i}{T} \right) \int (\hat{u}_{1,2} \hat{u}_{1,2}^* + \hat{v}_{1,2} \hat{v}_{1,2}^*) dy \tag{A15}$$

$$d_{21} = \int \left(\frac{d^2 \hat{u}_{1,1}}{dy^2} \hat{u}_{1,2}^* + \frac{d^2 \hat{v}_{1,1}}{dy^2} \hat{v}_{1,2}^* \right) dy \tag{A16}$$

$$d_{22} = \int \left(\frac{d^2 \hat{u}_{1,2}}{dy^2} \hat{u}_{1,2}^* + \frac{d^2 \hat{v}_{1,2}}{dy^2} \hat{v}_{1,2}^* \right) dy. \tag{A17}$$

4. Projection of thickness correction terms

The correction term of downstream evolution resulted by the scaling is

$$\begin{aligned}
\left\langle -\tilde{\mathbf{A}} \frac{\dot{g}}{g} y \frac{d\tilde{\mathbf{q}}}{dy}, \Phi_{1,1} \right\rangle &= -T \frac{\dot{g}}{g} \left[\int (u_0 \frac{d\hat{u}_{1,1}}{dy} \hat{u}_{1,1}^* + u_0 \frac{d\hat{v}_{1,1}}{dy} \hat{v}_{1,1}^*) y dy \right] a_{1,1} \\
&\quad - T \frac{\dot{g}}{g} \left[\int (u_0 \frac{d\hat{u}_{1,2}}{dy} \hat{u}_{1,1}^* + u_0 \frac{d\hat{v}_{1,2}}{dy} \hat{v}_{1,1}^*) y dy \right] a_{1,2} \\
&\quad - T \frac{\dot{g}}{g} \left[\int (\hat{u}_{1,1} \frac{du_0}{dy} \hat{u}_{1,1}^* + \hat{u}_{1,1} \frac{d\hat{v}_0}{dy} \hat{v}_{1,1}^*) y dy \right] a_{1,1} \\
&\quad - T \frac{\dot{g}}{g} \left[\int (\hat{u}_{1,2} \frac{du_0}{dy} \hat{u}_{1,1}^* + \hat{u}_{1,2} \frac{d\hat{v}_0}{dy} \hat{v}_{1,1}^*) y dy \right] a_{1,2} \\
&= T \frac{\dot{g}}{g} (e_{11} a_{1,1} + e_{12} a_{1,2}).
\end{aligned} \tag{A18}$$

Coefficients are

$$e_{11} = - \int (u_0 \frac{d\hat{u}_{1,1}}{dy} \hat{u}_{1,1}^* + u_0 \frac{d\hat{v}_{1,1}}{dy} \hat{v}_{1,1}^* + \hat{u}_{1,1} \frac{du_0}{dy} \hat{u}_{1,1}^*) y dy \quad (\text{A19})$$

$$e_{12} = - \int (u_0 \frac{d\hat{u}_{1,2}}{dy} \hat{u}_{1,1}^* + u_0 \frac{d\hat{v}_{1,2}}{dy} \hat{v}_{1,1}^* + \hat{u}_{1,2} \frac{du_0}{dy} \hat{u}_{1,1}^*) y dy, \quad (\text{A20})$$

where $\hat{v}_0 = 0$ is applied again. Similarly,

$$e_{21} = - \int (u_0 \frac{d\hat{u}_{1,1}}{dy} \hat{u}_{1,2}^* + u_0 \frac{d\hat{v}_{1,1}}{dy} \hat{v}_{1,2}^* + \hat{u}_{1,1} \frac{du_0}{dy} \hat{u}_{1,2}^*) y dy \quad (\text{A21})$$

$$e_{22} = - \int (u_0 \frac{d\hat{u}_{1,2}}{dy} \hat{u}_{1,2}^* + u_0 \frac{d\hat{v}_{1,2}}{dy} \hat{v}_{1,2}^* + \hat{u}_{1,2} \frac{du_0}{dy} \hat{u}_{1,2}^*) y dy. \quad (\text{A22})$$

5. Projection of external forcing terms

$$\begin{aligned} \langle f_{\tilde{\mathbf{q}}}, \Phi_{1,1} \rangle &= T \left[\int (A_{1,1} \hat{u}_{1,1} \hat{u}_{1,1}^* + A_{1,1} \hat{v}_{1,1} \hat{v}_{1,1}^*) dy \right] + T \left[\int (A_{1,2} \hat{u}_{1,2} \hat{u}_{1,1}^* + A_{1,2} \hat{v}_{1,2} \hat{v}_{1,1}^*) dy \right] \\ &= T(A_{1,1}). \end{aligned} \quad (\text{A23})$$

Similarly

$$\langle f_{\tilde{\mathbf{q}}}, \Phi_{1,2} \rangle = T(A_{1,2}). \quad (\text{A24})$$

6. Terms for thickness evolution

$$\begin{aligned} \left\langle y \tilde{u} \frac{\partial \tilde{u}}{\partial y}, y u_0 \frac{\partial u_0}{\partial y} \right\rangle &= T \int \left(y u_0 \frac{du_0}{dy} \right)^2 dy \\ &+ T \left[\int \left(\hat{u}_{1,1} \frac{d\hat{u}_{1,1}^*}{dy} + \hat{u}_{1,1}^* \frac{d\hat{u}_{1,1}}{dy} \right) y^2 u_0 \frac{du_0}{dy} dy \right] a_{1,1} a_{1,1}^* \\ &+ T \left[\int \left(\hat{u}_{1,1} \frac{d\hat{u}_{1,2}^*}{dy} + \hat{u}_{1,2}^* \frac{d\hat{u}_{1,1}}{dy} \right) y^2 u_0 \frac{du_0}{dy} dy \right] a_{1,1} a_{1,2}^* \\ &+ T \left[\int \left(\hat{u}_{1,2} \frac{d\hat{u}_{1,1}^*}{dy} + \hat{u}_{1,1}^* \frac{d\hat{u}_{1,2}}{dy} \right) y^2 u_0 \frac{du_0}{dy} dy \right] a_{1,2} a_{1,1}^* \\ &+ T \left[\int \left(\hat{u}_{1,2} \frac{d\hat{u}_{1,2}^*}{dy} + \hat{u}_{1,2}^* \frac{d\hat{u}_{1,2}}{dy} \right) y^2 u_0 \frac{du_0}{dy} dy \right] a_{1,2} a_{1,2}^*. \end{aligned} \quad (\text{A25})$$

and

$$\begin{aligned}
\left\langle f_g^1, yu_0 \frac{\partial u_0}{\partial y} \right\rangle &= \left\langle \mathcal{N}_g^1(\tilde{\mathbf{q}}, \tilde{\mathbf{q}}), yu_0 \frac{\partial u_0}{\partial y} \right\rangle + \left\langle \mathcal{L}_g^1(\tilde{\mathbf{q}}), yu_0 \frac{\partial u_0}{\partial y} \right\rangle \\
&= -Tg \left[\int (\hat{v}_{1,1} \frac{d\hat{u}_{1,1}^*}{dy} + \hat{v}_{1,1}^* \frac{d\hat{u}_{1,1}}{dy}) yu_0 \frac{du_0}{dy} dy \right] a_{1,1} a_{1,1}^* \\
&\quad - Tg \left[\int (\hat{v}_{1,1} \frac{d\hat{u}_{1,2}^*}{dy} + \hat{v}_{1,2}^* \frac{d\hat{u}_{1,1}}{dy}) yu_0 \frac{du_0}{dy} dy \right] a_{1,1} a_{1,2}^* \\
&\quad - Tg \left[\int (\hat{v}_{1,2} \frac{d\hat{u}_{1,1}^*}{dy} + \hat{v}_{1,1}^* \frac{d\hat{u}_{1,2}}{dy}) yu_0 \frac{du_0}{dy} dy \right] a_{1,2} a_{1,1}^* \\
&\quad - Tg \left[\int (\hat{v}_{1,2} \frac{d\hat{u}_{1,2}^*}{dy} + \hat{v}_{1,2}^* \frac{d\hat{u}_{1,2}}{dy}) yu_0 \frac{du_0}{dy} dy \right] a_{1,2} a_{1,2}^* \\
&\quad + \frac{1}{Re} g^2 T \int \left(\frac{d^2 u_0}{dy^2} yu_0 \frac{du_0}{dy} dy \right).
\end{aligned} \tag{A26}$$

Therefore, the coefficients in thickness evolution equation (36) are

$$b_0 = \int \left(yu_0 \frac{du_0}{dy} \right)^2 dy \tag{A27}$$

$$b_{01} = \int \left(\hat{u}_{1,1} \frac{d\hat{u}_{1,1}^*}{dy} + \hat{u}_{1,1}^* \frac{d\hat{u}_{1,1}}{dy} \right) y^2 u_0 \frac{du_0}{dy} dy \tag{A28}$$

$$b_{02} = \int \left(\hat{u}_{1,1} \frac{d\hat{u}_{1,2}^*}{dy} + \hat{u}_{1,2}^* \frac{d\hat{u}_{1,1}}{dy} \right) y^2 u_0 \frac{du_0}{dy} dy \tag{A29}$$

$$b_{03} = \int \left(\hat{u}_{1,2} \frac{d\hat{u}_{1,1}^*}{dy} + \hat{u}_{1,1}^* \frac{d\hat{u}_{1,2}}{dy} \right) y^2 u_0 \frac{du_0}{dy} dy \tag{A30}$$

$$b_{04} = \int \left(\hat{u}_{1,2} \frac{d\hat{u}_{1,2}^*}{dy} + \hat{u}_{1,2}^* \frac{d\hat{u}_{1,2}}{dy} \right) y^2 u_0 \frac{du_0}{dy} dy \tag{A31}$$

$$c_{01} = - \int \left(\hat{v}_{1,1} \frac{d\hat{u}_{1,1}^*}{dy} + \hat{v}_{1,1}^* \frac{d\hat{u}_{1,1}}{dy} \right) yu_0 \frac{du_0}{dy} dy \tag{A32}$$

$$c_{02} = - \int \left(\hat{v}_{1,1} \frac{d\hat{u}_{1,2}^*}{dy} + \hat{v}_{1,2}^* \frac{d\hat{u}_{1,1}}{dy} \right) yu_0 \frac{du_0}{dy} dy \tag{A33}$$

$$c_{03} = - \int \left(\hat{v}_{1,2} \frac{d\hat{u}_{1,1}^*}{dy} + \hat{v}_{1,1}^* \frac{d\hat{u}_{1,2}}{dy} \right) yu_0 \frac{du_0}{dy} dy \tag{A34}$$

$$c_{04} = - \int \left(\hat{v}_{1,2} \frac{d\hat{u}_{1,2}^*}{dy} + \hat{v}_{1,2}^* \frac{d\hat{u}_{1,2}}{dy} \right) yu_0 \frac{du_0}{dy} dy \tag{A35}$$

$$d_0 = \int \left(\frac{d^2 u_0}{dy^2} \right) yu_0 \frac{du_0}{dy} dy. \tag{A36}$$

and the differential equations for scaling variable g and coefficient vector are

$$\begin{aligned}
\mathbf{a} &= (a_{1,1} \quad a_{1,2})^T \\
\dot{g} &= \frac{(c_{01} a_{1,1} a_{1,1}^* + c_{02} a_{1,1} a_{1,2}^* + c_{03} a_{1,2} a_{1,1}^* + c_{04} a_{1,2} a_{1,2}^*) g^2 + \frac{1}{Re} d_0 g^3}{b_0 + b_{01} a_{1,1} a_{1,1}^* + b_{02} a_{1,1} a_{1,2}^* + b_{03} a_{1,2} a_{1,1}^* + b_{04} a_{1,2} a_{1,2}^*},
\end{aligned} \tag{A37}$$

and

$$\mathbf{B}\dot{\mathbf{a}} = (g\mathbf{C} + \boldsymbol{\Lambda} + \frac{1}{\text{Re}}g^2\mathbf{D} + \frac{\dot{g}}{g}\mathbf{E})\mathbf{a} + \mathbf{F}. \quad (\text{A38})$$

where the matrices $\mathbf{B}, \mathbf{C}, \boldsymbol{\Lambda}, \mathbf{D}, \mathbf{E}$, and \mathbf{F} for the two mode case were defined previously in section IV D.

Appendix B: Equations for the 4-mode model

The differential equations for scaling variable g and coefficient vector

$$\mathbf{a} = (a_{1,1} \ a_{1,2} \ a_{2,1} \ a_{2,2})^T$$

for 4-mode model are given as

$$\dot{g} = \frac{C_0}{B_0}g^2 + \frac{1}{\text{Re}}\frac{d_0}{B_0}g^3 \quad (\text{B1})$$

where coefficients B_0 and C_0 are given as

$$\begin{aligned} B_0 = & b_0 + b_{01}a_{1,1}a_{1,1}^* + b_{02}a_{1,1}a_{1,2}^* + b_{03}a_{1,2}a_{1,1}^* + b_{04}a_{1,2}a_{1,2}^* \\ & + b_{05}a_{2,1}a_{2,1}^* + b_{06}a_{2,1}a_{2,2}^* + b_{07}a_{2,2}a_{2,1}^* + b_{08}a_{2,2}a_{2,2}^*, \end{aligned} \quad (\text{B2})$$

$$\begin{aligned} C_0 = & c_{01}a_{1,1}a_{1,1}^* + c_{02}a_{1,1}a_{1,2}^* + c_{03}a_{1,2}a_{1,1}^* + c_{04}a_{1,2}a_{1,2}^* \\ & + c_{05}a_{2,1}a_{2,1}^* + c_{06}a_{2,1}a_{2,2}^* + c_{07}a_{2,2}a_{2,1}^* + c_{08}a_{2,2}a_{2,2}^*, \end{aligned} \quad (\text{B3})$$

and

$$\mathbf{B}\dot{\mathbf{a}} = (\mathbf{C} + \frac{g^2}{\text{Re}}\mathbf{D} + \frac{\dot{g}}{g}\mathbf{E})\mathbf{a} + \mathbf{N}_1 + \frac{\dot{g}}{g}\mathbf{N}_2 + \mathbf{F}, \quad (\text{B4})$$

where matrices \mathbf{N}_1 and \mathbf{N}_2 includes all terms nonlinear to $a_{k,n}$ as

$$\mathbf{N}_1 = \begin{bmatrix} g(c_{1121}a_{1,1}^*a_{2,1} + c_{1122}a_{1,1}^*a_{2,2} + c_{1221}a_{1,2}^*a_{2,1} + c_{1222}a_{1,2}^*a_{2,2}) \\ g(c_{1321}a_{1,1}^*a_{2,1} + c_{1322}a_{1,1}^*a_{2,2} + c_{1421}a_{1,2}^*a_{2,1} + c_{1422}a_{1,2}^*a_{2,2}) \\ g(c_{1511}a_{1,1}a_{1,1} + c_{1512}a_{1,1}a_{1,2} + c_{1522}a_{1,2}a_{1,2}) \\ g(c_{1611}a_{1,1}a_{1,1} + c_{1612}a_{1,1}a_{1,2} + c_{1622}a_{1,2}a_{1,2}) \end{bmatrix}, \quad (\text{B5})$$

and

$$\mathbf{N}_2 = \begin{bmatrix} e_{1121}a_{1,1}^*a_{2,1} + e_{1122}a_{1,1}^*a_{2,2} + e_{1221}a_{1,2}^*a_{2,1} + c_{1222}a_{1,2}^*a_{2,2} \\ e_{1321}a_{1,1}^*a_{2,1} + e_{1322}a_{1,1}^*a_{2,2} + e_{1421}a_{1,2}^*a_{2,1} + c_{1422}a_{1,2}^*a_{2,2} \\ e_{1511}a_{1,1}a_{1,1} + e_{1512}a_{1,1}a_{1,2} + e_{1522}a_{1,2}a_{1,2} \\ e_{1611}a_{1,1}a_{1,1} + e_{1612}a_{1,1}a_{1,2} + e_{1622}a_{1,2}a_{1,2} \end{bmatrix}, \quad (\text{B6})$$

and other matrices for terms linear to $a_{k,n}$ have blocks of zeroes as shown below:

$$\begin{aligned} \mathbf{B} &= \begin{bmatrix} \mathbf{B}_1 & 0 \\ 0 & \mathbf{B}_2 \end{bmatrix}, & \mathbf{C} &= \begin{bmatrix} \mathbf{C}_1 & 0 \\ 0 & \mathbf{C}_2 \end{bmatrix}, & \mathbf{D} &= \begin{bmatrix} \mathbf{D}_1 & 0 \\ 0 & \mathbf{D}_2 \end{bmatrix}, \\ \mathbf{E} &= \begin{bmatrix} \mathbf{E}_1 & 0 \\ 0 & \mathbf{E}_2 \end{bmatrix}, & \mathbf{F} &= \begin{bmatrix} A_{1,1} \\ A_{1,2} \\ A_{2,1} \\ A_{2,2} \end{bmatrix}, \end{aligned} \tag{B7}$$

with sub-matrices defined by

$$\begin{aligned} \mathbf{B}_1 &= \begin{bmatrix} b_{111} & b_{112} \\ b_{211} & b_{212} \end{bmatrix}, & \mathbf{B}_2 &= \begin{bmatrix} b_{121} & b_{122} \\ b_{221} & b_{222} \end{bmatrix}, \\ \mathbf{C}_1 &= \begin{bmatrix} gc_{111} + c_{311} & gc_{112} \\ gc_{211} & gc_{212} + c_{312} \end{bmatrix}, & \mathbf{C}_2 &= \begin{bmatrix} gc_{121} + c_{321} & gc_{122} \\ gc_{221} & gc_{222} + c_{322} \end{bmatrix}, \\ \mathbf{D}_1 &= \begin{bmatrix} d_{111} & d_{112} \\ d_{211} & d_{212} \end{bmatrix}, & \mathbf{D}_2 &= \begin{bmatrix} d_{121} & d_{122} \\ d_{221} & d_{222} \end{bmatrix}, \\ \mathbf{E}_1 &= \begin{bmatrix} e_{111} & e_{112} \\ e_{211} & e_{212} \end{bmatrix}, & \mathbf{E}_2 &= \begin{bmatrix} e_{121} & e_{122} \\ e_{221} & e_{222} \end{bmatrix}. \end{aligned}$$

The equations for coefficients are too many to be listed here.

REFERENCES

- ¹P. G. Saffman and G. R. Baker, ‘‘Vortex interactions,’’ *Ann. Rev. Fluid Mech.* **11**, 95–122 (1979).
- ²C. M. Ho and P. Huerre, ‘‘Perturbed free shear layers,’’ *Ann. Rev. Fluid Mech.* **16**, 365–424 (1984).
- ³P. J. Schmid and D. S. Henningson, *Stability and Transition in Shear Flows*, Applied Mathematical Sciences, Vol. 142 (Springer-Verlag, 2001).
- ⁴J.-M. Chomaz, ‘‘Global instabilities in spatially developing flows: non-normality and non-linearity,’’ *Ann. Rev. Fluid Mech.* **37**, 357–392 (2005).
- ⁵J. S. Baggett and L. N. Trefethen, ‘‘Low-dimensional models of subcritical transition to turbulence,’’ *Phys. Fluids* **9**, 1043–1053 (1997).

- ⁶M. Wei and C. W. Rowley, “Low-dimensional models of a temporally evolving free shear layer,” *J. Fluid Mech.* **618**, 113–134 (2009).
- ⁷C. W. Rowley and J. E. Marsden, “Reconstruction equations and the Karhunen-Loève expansion for systems with symmetry,” *Phys. D* **142**, 1–19 (2000).
- ⁸C. W. Rowley, I. G. Kevrekidis, J. E. Marsden, and K. Lust, “Reduction and reconstruction for self-similar dynamical systems,” *Nonlinearity* **16**, 1257–1275 (2003).
- ⁹M. Wei, B. R. Qawasmeh, M. B. Barone, and B. G. van Bloemen Waanders, “Low-dimensional modeling for spatial developing free shear layers,” 47th AIAA Aerospace Sciences Meeting and Exhibit, Orlando, FL, AIAA Paper 2009-363 (2009).
- ¹⁰T. Herbert, “Parabolized stability equations,” *Annual Review of Fluid Mechanics* **29**, 245–283 (1997).
- ¹¹S. G. Rubin and J. C. Tannehill, “Parabolized/reduced navier-stokes computational techniques,” *Annual Review of Fluid Mechanics* **24**, 117–144 (1992).
- ¹²H. Schlichting and K. Gersten, *Boundary-Layer Theory*, 8th ed. (Springer-Verlag, Berlin, 2000) pp. 126–128.
- ¹³X. Shi, O. M. Knio, and J. Katz, “Numerical study of shear-induced heating in high-speed nozzle flow of liquid monopropellant,” *Journal of Heat Transfer* **120**, 58–64 (1998).
- ¹⁴C.-M. Ho and L.-S. Huang, “Subharmonics and vortex merging in mixing layers,” *J. Fluid Mech.* **119**, 443–473 (1982).
- ¹⁵R. W. Miksad, “Experiments on the nonlinear stages of free-shear-layer transition,” *Journal of Fluid Mechanics* **56**, 695–719 (1972).
- ¹⁶R. W. Miksad, “Experiments on nonlinear interactions in the transition of a free shear layer,” *J. Fluid Mech.* **59**, 1–21 (1973).
- ¹⁷C.-M. Ho and Y. Q. Zhang, “On the manipulation of spreading rates of forced mixing layers,” In Proc. 3rd Int. Symp. on Turbulent Shear Flows, University of California, Davis (1981).
- ¹⁸G. L. Brown and A. Roshko, “On density effects and large structure in turbulent mixing layers,” *J. Fluid Mech.* **64**, 775–816 (1974).
- ¹⁹M. Wei and J. B. Freund, “A noise-controlled free shear flow,” *J. Fluid Mech.* **546**, 123–152 (2006).
- ²⁰P. A. Monkewitz and P. Huerre, “Influence of the velocity ratio on the spatial instability of mixing layers,” *Phys. Fluids* **25**, 1137–1143 (1982).

- ²¹F. M. White, *Viscous Fluid Flow*, 3rd ed. (McGraw-Hill, Inc., New York, 2006).
- ²²D. G. Crighton and M. Gaster, “Stability of slowly diverging jet flow,” *J. Fluid Mech.* **88**, 397–413 (1976).
- ²³P. Huerre and M. Rossi, “Hydrodynamic instabilities in open flows,” in *Hydrodynamics and nonlinear instabilities*, edited by C. Godréche and P. Manneville (Cambridge University Press, 1998) pp. 81–294.
- ²⁴M. Wei and C. W. Rowley, “Low-dimensional models of a temporally evolving free shear layer,” 36th AIAA Fluid Dynamics Conference and Exhibit, 5-8 June 2006, San Francisco, AIAA Paper 2006-3228 (2006).
- ²⁵R. E. Kelly, “On the stability of an inviscid shear layer which is periodic in space and time,” *Journal of Fluid Mechanics* **27**, 657–689 (1967).
- ²⁶D. E. Nikitopoulos and J. T. C. Liu, “Nonlinear binary-mode interactions in a developing mixing layer,” *Journal of Fluid Mechanics* **179**, 345–370 (1987).
- ²⁷J. Ko, D. Lucor, and P. Sagaut, “Sensitivity of two-dimensional spatially developing mixing layers with respect to uncertain inflow conditions,” *Physics of Fluids* **20**, 077102 (2008).